Extreme Mechanics Letters 81 (2025) 102412

Contents lists available at ScienceDirect

Extreme Mechanics Letters

journal homepage: www.elsevier.com/locate/eml

The nonlinear elastic response of magnetorheological elastomers

Chao Wang [a], Yingqi Jia [a], Arvin Ardebili Sharma [b], Zhi Zhao [a], Xiaojia Shelly Zhang [a,c,d,*]

[a] Department of Civil and Environmental Engineering, University of Illinois Urbana-Champaign, Urbana, IL 61801, USA
[b] Department of Materials Science and Engineering, University of Illinois Urbana-Champaign, Urbana, IL 61801, USA
[c] Department of Mechanical Science and Engineering, University of Illinois Urbana-Champaign, Urbana, IL 61801, USA
[d] National Center for Supercomputing Applications, Urbana, IL 61801, USA

ARTICLE INFO

Keywords:
Magnetorheological elastomers (MREs)
Rigid inclusions
Incompressibility
Finite deformations
Homogenization
Experimental validation

ABSTRACT

Magnetorheological elastomers (MREs), consisting of a soft elastomeric matrix embedded with rigid (and typically magnetized) particles such as NdFeB, are increasingly used in mechanical and biomedical applications. Accurate modeling of their magneto-mechanical behavior requires first predicting their purely mechanical response. Traditionally, this mechanical prediction has relied on directly measuring the macroscopic response of MREs, either numerically or experimentally, for each particle fraction of interest, a procedure that is both time-consuming and labor-intensive. In this study, we replace that procedure with a simple computational framework that requires only a single measurement on the unfilled elastomer. The framework treats MREs as general incompressible filled elastomers and predicts their nonlinear elastic response by integrating several established modeling techniques. For any physically admissible particle volume fraction, it analytically predicts the macroscopic nonlinear response from the measured properties of the unfilled elastomer. We validate the framework experimentally across a wide range of cross-link densities in the elastomeric matrices, particle volume fractions (0%–28%), and specimen geometries, subjected to both uniform and highly localized large deformations (with local strains up to ~600%). The experimental results show excellent agreement with the computational predictions, confirming the framework as a fast and reliable tool for predicting the nonlinear elastic response of MREs. Consequently, this study offers a practical tool for streamlining the modeling and design of MRE-based structures.

1. Introduction

Magnetorheological elastomers (MREs) are soft elastomeric matrices embedded with rigid magnetic particles, which can be either magnetically soft (e.g., iron and iron oxides [1,2]) or hard (e.g., neodymium–iron–boron or NdFeB [3,4]). Recently, they have attracted significant attention because they undergo large mechanical deformations under external, contactless magnetic stimuli. This property makes MREs promising for diverse applications, including wireless biomedical devices [3,5,6], vibration isolators [7], sensors and actuators [8,9], and magneto-mechanical robots [10–12].

To fully exploit the capabilities of MREs and optimize their design, accurate modeling of their magneto-mechanical behavior is essential and has been extensively studied [1,4,13–18]. A fundamental ingredient in such coupled frameworks is the description of the purely mechanical response. Most existing studies employ hyperelastic formulations, relying on computational or experimental homogenization to capture the composite response without explicitly separating the roles of the elastomeric matrix and the magnetic particles. As a result, the mechanical behavior must be characterized for each particle volume fraction of interest, which can be an inefficient and laborious process.

To address this issue, a more promising approach is to explicitly account for the contributions of both matrix and particles through analytical homogenization. From this perspective, non-magnetized MREs reduce to general filled elastomers, a well-studied class of materials where rigid fillers like carbon black or silica increase elastomer stiffness [19]. The analytical homogenization of filled elastomers has a long and rich history, tracing back to classical works such as [20–23]. Among the existing studies, we highlight the work of [24,25]. In [24], an exact solution was derived for the nonlinear elastic response of Gaussian (neo-Hookean) rubber reinforced by a dilute, isotropic distribution of rigid particles. The companion study [25] extended these results to non-Gaussian elastomers and finite particle concentrations, with *numerical* verification over particle fractions of 5%–25%.

Despite these advances, the applicability of [25] to non-magnetized MREs remains uncertain because of the lack of direct *experimental* validation. The closest experiment comes from Leonard et al. [26],

* Corresponding author at: Department of Civil and Environmental Engineering, University of Illinois Urbana-Champaign, Urbana, IL 61801, USA.
E-mail address: zhangxs@illinois.edu (X.S. Zhang).

https://doi.org/10.1016/j.eml.2025.102412
Received 7 August 2025; Received in revised form 11 September 2025; Accepted 11 October 2025
Available online 14 October 2025

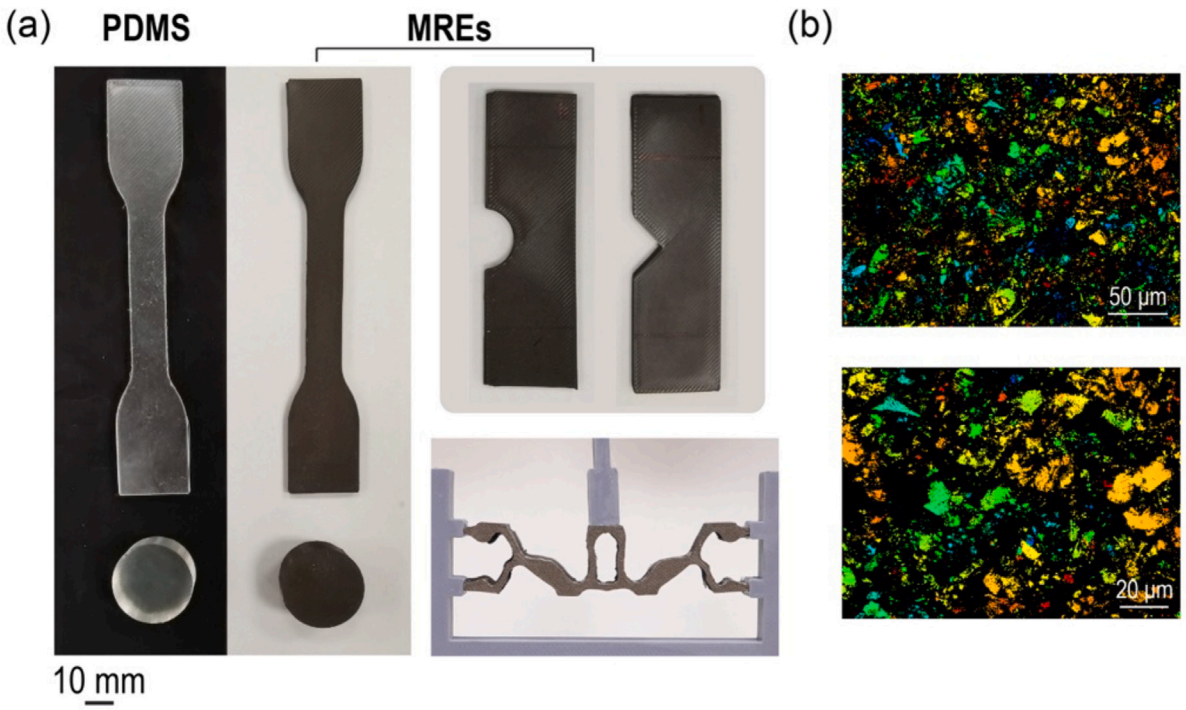

Fig. 1. Fabricated specimens for mechanical testing. (a) Photographs of dog-bone-shaped specimens composed of pure PDMS and MREs. (b) Optical microscopy images of a representative MRE sample (20:1 PDMS with 28 vol% NdFeB particles) at 20 and 50 μm magnifications, showing the uniform dispersion of rigid particles within the elastomer matrix.

who tested rectangular elastomers filled with glass spheres at a single particle fraction (10%) under uniaxial tension. However, MREs differ substantially in that MREs

- employ magnetizable particles (e.g., iron oxide or NdFeB) rather than glass;
- contain irregularly shaped particles (see the microscopic images in Fig. 1(b)), not near-perfect spheres;
- span a wide range of particle fractions, rather than a single concentration of 10%;
- feature diverse geometries, from simple rectangles to topologically optimized designs [8,9,12];
- undergo complex loading conditions beyond uniaxial tension.

Therefore, pedigreed experimental data are still lacking to validate analytical homogenization approaches (such as [25]) for predicting the nonlinear elastic response of MREs.

In this work, we pursue two objectives: (1) to integrate established theoretical results into a complete computational framework for predicting the nonlinear elastic response of non-magnetized MREs, and (2) to provide systematic experimental validation of this framework. On the theoretical side, we adopt the effective non-Gaussian stored-energy function from [27], a more general formulation than [25], to describe nonlinear elastic responses. This model further relies on the initial shear modulus ratio (γ_0) between filled (used as a comparison medium) and unfilled Gaussian elastomers. To compute the ratio γ_0, we employ the explicit formula from [19], which is validated from the dilute limit to the percolation threshold. Additionally, to account for the incompressibility of MREs, we formulate the equilibrium equations in mixed form, readily implementable in the open-source FEniCSx platform [28].

For experimental validation, we fabricate and test a series of representative MRE samples featuring

- polydimethylsiloxane (PDMS) matrices with base-to-agent ratios of 10:1, 20:1, and 25:1, representing different cross-link densities;
- magnetizable NdFeB particles at volume fractions of 0%, 11%, 17%, and 28%;
- diverse geometries, including dog-bone, cylindrical, round-notched, V-notched, and topologically optimized designs, subjected to both uniform (uniaxial tension and compression) and highly localized deformations (local strains up to ~600%).

The experimental results align well with the computational predictions, thereby confirming the validity of the integrated framework. With this validated approach, the macroscopic mechanical response of MREs can be directly predicted for any physically admissible particle volume fraction using only a single measurement of the elastomeric matrix, eliminating the need for repeated computational or experimental homogenization. Moreover, the framework lays the foundation for rapid prediction of magneto-mechanical responses when embedded into coupled formulations [4,29,30], thus accelerating the design of magnetically actuated soft devices.

The remainder of this paper is organized as follows. Section 2 presents the computational framework, including the constitutive model for MREs and its numerical implementation that imposes *perfect* incompressibility. Section 3 validates the framework through the fabrication and testing of representative MRE samples. Section 4 concludes with remarks and future directions. Appendix A outlines the derivation from [25] for the stored-energy function of general filled elastomers, while Appendix B derives the equilibrium equations for *nearly* incompressible MREs.

2. Computational framework for modeling MREs

In this section, we present the integrated computational framework for modeling MREs. We begin by reviewing a constitutive model for MREs developed in [19,27], followed by its numerical implementation, which employs a mixed formulation to enforce perfect incompressibility.

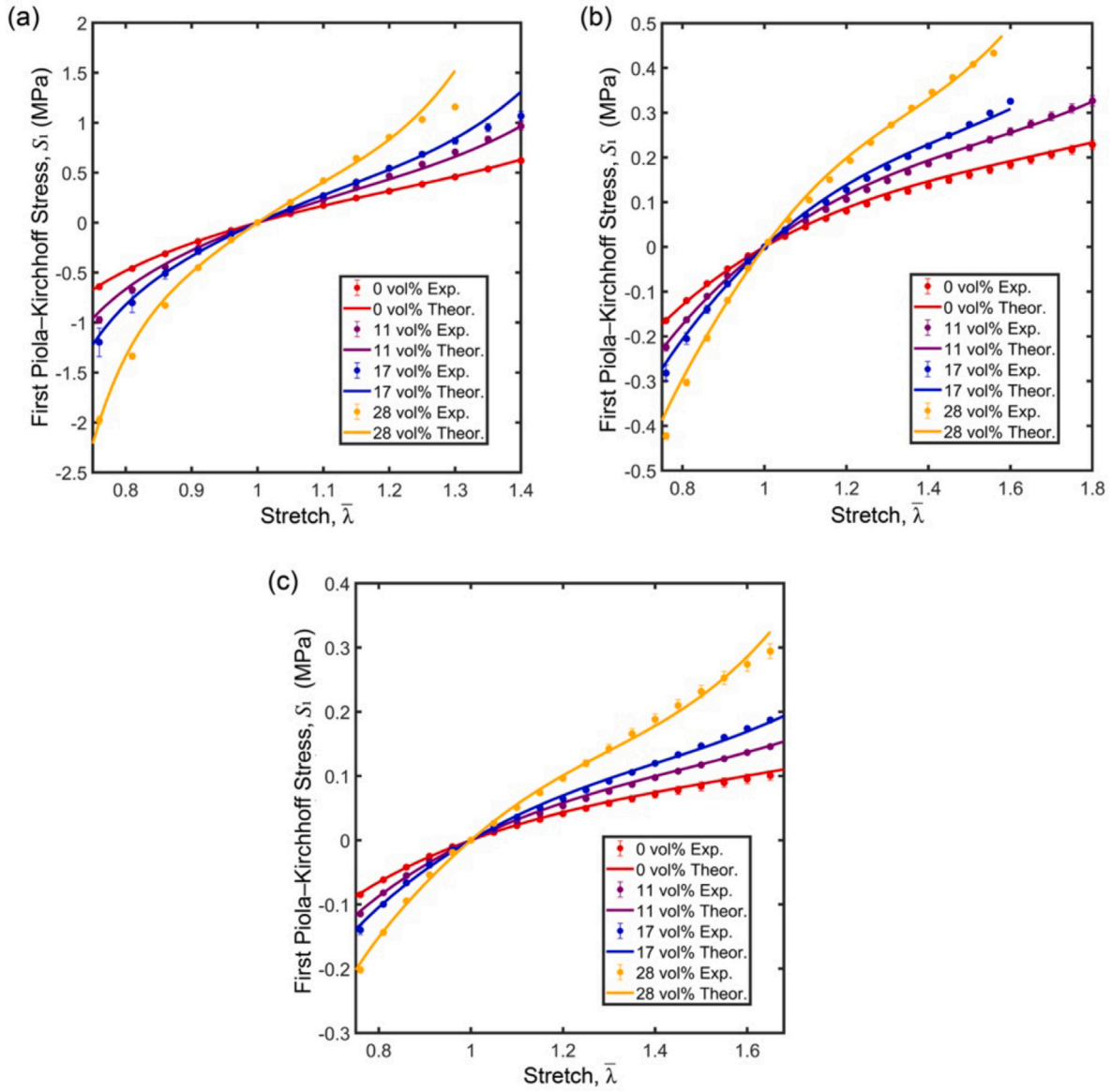

Fig. 2. Comparisons between theoretical predictions and experimental measurements of the uniaxial stress–stretch (S_1–$\bar{\lambda}$) response of MREs. Solid curves represent the theoretical predictions based on (6), while discrete markers with error bars indicate the experimental data. Results are presented for (a) Group 1 (10:1 PDMS), (b) Group 2 (20:1 PDMS), and (c) Group 3 (25:1 PDMS), each with varying NdFeB particle volume fractions.

2.1. Constitutive model of MREs

In this subsection, we recap the constitutive model used to predict the elastic response of MREs. We idealize the MRE as a composite of

- an isotropic, incompressible, elastic, and non-Gaussian matrix with the stored-energy function [31]

$$\psi(I_1) = \begin{cases} \displaystyle\sum_{r=1}^{2} \frac{3^{1-\alpha_r}}{2\alpha_r}\mu_r\left(I_1^{\alpha_r} - 3^{\alpha_r}\right) & \text{if } \det(\mathbf{F}) = 1 \\ +\infty & \text{otherwise,} \end{cases} \tag{1}$$

- firmly embedding rigid, spherical, and non-overlapping particles of approximately uniform size, with the stored-energy function

$$\psi_{\mathrm{p}}(\mathbf{F}) = \begin{cases} 0 & \text{if } \mathbf{F} \in \mathrm{Orth}^{+} \\ +\infty & \text{otherwise,} \end{cases} \tag{2}$$

- where the particle distribution is random yet isotropic.

Here, $I_1 = \mathbf{F} : \mathbf{F}$, with $\mathbf{F} = \mathbf{I} + \nabla\mathbf{u}$ denoting the deformation gradient and $\mathbf{u}$ the displacement field. The parameters α_1, α_2, μ_1, and μ_2 are determined experimentally, and the initial shear modulus of the matrix is $\mu = \mu_1 + \mu_2$. The set Orth^{+} denotes proper orthogonal second-order tensors. The definition of ψ_{p} ensures that rigid particles undergo pure rotations without stretching, contributing no strain energy under admissible deformations.

Based on this idealization, the macroscopic (effective) elastic response of MREs is expressed by the stored-energy function

$$\overline{\psi}_c(\bar{I}_1; c) = \begin{cases} (1-c)\psi\left(\dfrac{\gamma_0}{1-c}(\bar{I}_1 - 3) + 3\right) & \text{if } \det(\overline{\mathbf{F}}) = 1 \\ +\infty & \text{otherwise} \end{cases} \tag{3}$$

following Eqs. (64) and (67) of [27]. Here, $\bar{I}_1 = \overline{\mathbf{F}} : \overline{\mathbf{F}}$ is the macroscopic invariant, $\overline{\mathbf{F}}$ is the macroscopic deformation gradient, and c is the particle volume fraction. The parameter γ_0 is the initial shear modulus ratio between the filled elastomer (used as a comparison medium; see details in [27]) and its underlying Gaussian matrix material. According

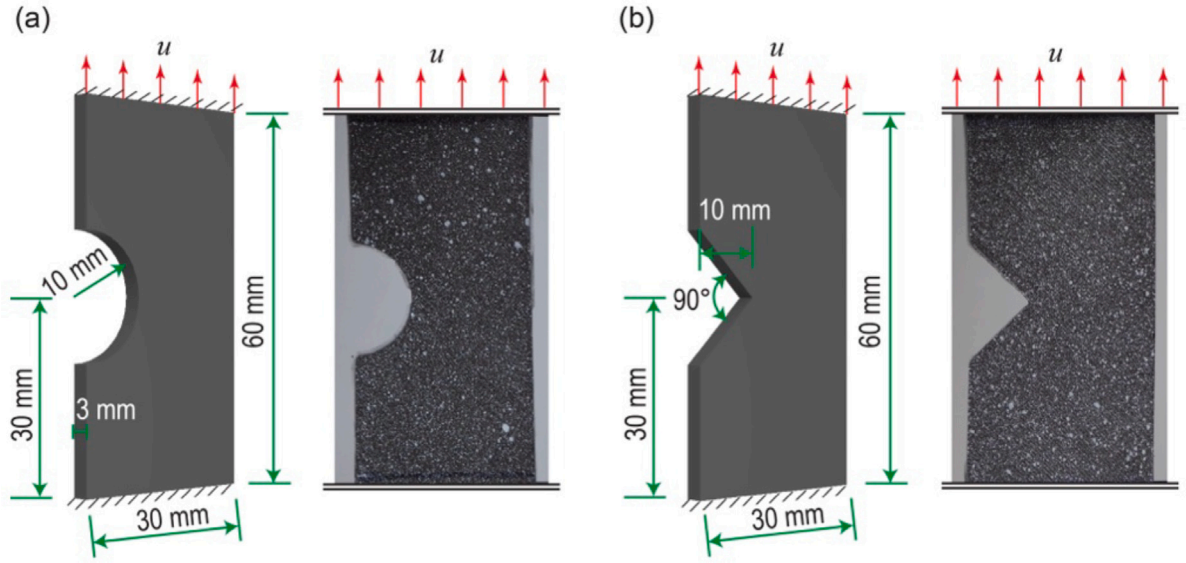

Fig. 3. Illustrative and fabricated notched specimens used for testing localized strain responses. (a) Specimen with the round notch. (b) Specimen with the V-shaped notch.

to Eq. (10) of [19], we write out

$$\gamma_0 = \left\{\left[1+\gamma_1\left(\gamma_2+\gamma_3^2\right)\gamma_3^2\right]\left(1-\gamma_3\right)\right\}^{-\frac{5}{2}\gamma_4} \tag{4}$$

with $\gamma_1 = 0.635$, $\gamma_2 = 0.027$, $\gamma_3 = c/\gamma_4$, and $\gamma_4 = 0.640$.

Finally, substituting (1) into (3) yields the explicit stored-energy function

$$\widetilde{\psi}_c(\overline{I}_1; c) = \begin{cases} (1-c)\displaystyle\sum_{r=1}^{2}\frac{3^{1-\alpha_r}}{2\alpha_r}\mu_r\left\{\left[\frac{\gamma_0(\overline{I}_1-3)}{1-c}+3\right]^{\alpha_r}-3^{\alpha_r}\right\} & \text{if } \det(\overline{\mathbf{F}})=1 \\ +\infty & \text{otherwise.} \end{cases} \tag{5}$$

Under uniaxial loading with principal stretches $\overline{\lambda}_1 = \overline{\lambda}$ and $\overline{\lambda}_2 = \overline{\lambda}_3 = \overline{\lambda}^{-1/2}$, the principal first Piola–Kirchhoff stress takes the form

$$S_1(\overline{\lambda}; c) = \frac{\partial\widetilde{\psi}_c}{\partial\overline{I}_1}\frac{\partial\overline{I}_1}{\partial\overline{\lambda}_1} = \gamma_0\left(\overline{\lambda}-\overline{\lambda}^{-2}\right)\sum_{r=1}^{2}3^{1-\alpha_r}\mu_r\left[\frac{\gamma_0\left(\overline{\lambda}^{-2}+2\overline{\lambda}^{-1}-3\right)}{(1-c)}+3\right]^{\alpha_r-1}, \tag{6}$$

where $\overline{\lambda}$ is the applied stretch, and $\overline{I}_1 = \overline{\lambda}_1^2+\overline{\lambda}_2^2+\overline{\lambda}_3^2 = \overline{\lambda}^2+2\overline{\lambda}^{-1}$.

Remark 1. The advantage of the material model in (5) merits explicit clarification. The stored-energy function in (5) enables direct predictions of the macroscopic response of MREs using only the constitutive parameters (α_1, α_2, μ_1, and μ_2) of the base elastomer in (1) and the filler volume fraction (c). This feature bypasses the need to fabricate and test reinforced specimens for each c value, offering an efficient tool for characterizing the mechanical responses of MREs.

Remark 2. The material model for MREs in (5) reduces exactly to the unfilled elastomer model in (1) when the filler is absent ($c = 0$). This can be proved by examining $\widetilde{\psi}_c(\overline{I}_1; 0) \equiv \psi(\overline{I}_1)$ for any choice of $\overline{I}_1$.

Remark 3. The expression for γ_0 in (4) applies to all feasible particle volume fractions, from the dilute limit ($c \searrow 0\%$) up to the percolation threshold ($c \nearrow \gamma_4 = 64\%$, assuming uniform particle diameters) [19]. Alternative formulae for γ_0 can also be used. For instance, adopting

$$\gamma_0 = (1-c)^{-5/2}$$

derived from the classical differential scheme [32], reduces (3) to

$$\widehat{\psi}_c(\overline{I}_1; c) = \begin{cases} (1-c)\psi\left(\dfrac{\overline{I}_1-3}{(1-c)^{7/2}}+3\right) & \text{if } \det(\overline{\mathbf{F}})=1 \\ +\infty & \text{otherwise,} \end{cases} \tag{7}$$

which coincides with Eq. (49) of [25] and has been numerically verified for particle volume fractions $c \in [5\%, 25\%]$. Appendix A summarizes the key derivation steps of (7) for interested readers.

2.2. Numerical implementation

After presenting the constitutive model in (5), we implement it numerically to predict the elastic response of MREs. To enforce the *perfect* incompressibility constraint, we write the Lagrangian form of (5) as

$$\mathcal{L}(\overline{I}_1, \widehat{p}; c) = \widetilde{\psi}_c(\overline{I}_1; c) + \widehat{p}\,(\overline{J}-1),$$

where $\widehat{p}$ is the Lagrange multiplier and $\overline{J} = \det(\overline{\mathbf{F}})$.

Applying the principle of minimum potential energy leads to the weak form of the equilibrium equations

$$\begin{cases} r_u(\mathbf{u}, \widehat{p}) = \displaystyle\int_{\Omega^0}\left(2\widetilde{\psi}_{c,\overline{I}_1}\overline{\mathbf{F}} + \widehat{p}\,\overline{J}\,\overline{\mathbf{F}}^{-\top}\right) : \nabla\mathbf{v}\,\mathrm{d}\mathbf{X} - \int_{\Omega^0}\overline{\mathbf{b}}\cdot\mathbf{v}\,\mathrm{d}\mathbf{X} \\ \quad - \displaystyle\int_{\partial\Omega^0_{\mathcal{N}}}\overline{\mathbf{t}}\cdot\mathbf{v}\,\mathrm{d}\mathbf{X} = 0 \quad \forall\mathbf{v}\in\mathcal{K} \\ r_p(\mathbf{u}) = \displaystyle\int_{\Omega^0}\left(\overline{J}-1\right)\widehat{q}\,\mathrm{d}\mathbf{X} = 0 \quad \forall\widehat{q}\in\mathcal{Q} \end{cases} \tag{8}$$

subject to $\mathbf{u} = \overline{\mathbf{u}}$ on $\partial\Omega^0_D$. Here, r_u and r_p are the residuals to be enforced as zero. Ω^0 is the undeformed, stress-free configuration of the MRE, with $\partial\Omega^0_D$ and $\partial\Omega^0_{\mathcal{N}}$ denoting the Dirichlet and Neumann boundaries, respectively. The variable $\mathbf{u}$ is the displacement field, and $\overline{\mathbf{F}} = \mathbf{I} + \nabla\mathbf{u}$. The variables $\overline{\mathbf{b}}$, $\overline{\mathbf{t}}$, and $\overline{\mathbf{u}}$ are the prescribed body force, traction, and displacement, respectively. $\mathbf{v}$ and $\widehat{q}$ are the test functions corresponding to $\mathbf{u}$ and $\widehat{p}$, respectively, and $\mathcal{K}$ and $\mathcal{Q}$ denote the associated kinematically admissible function spaces.

Remark 4. The weak form in (8) corresponds to *perfectly* incompressible MREs. For *nearly* incompressible MREs, Appendix B summarizes

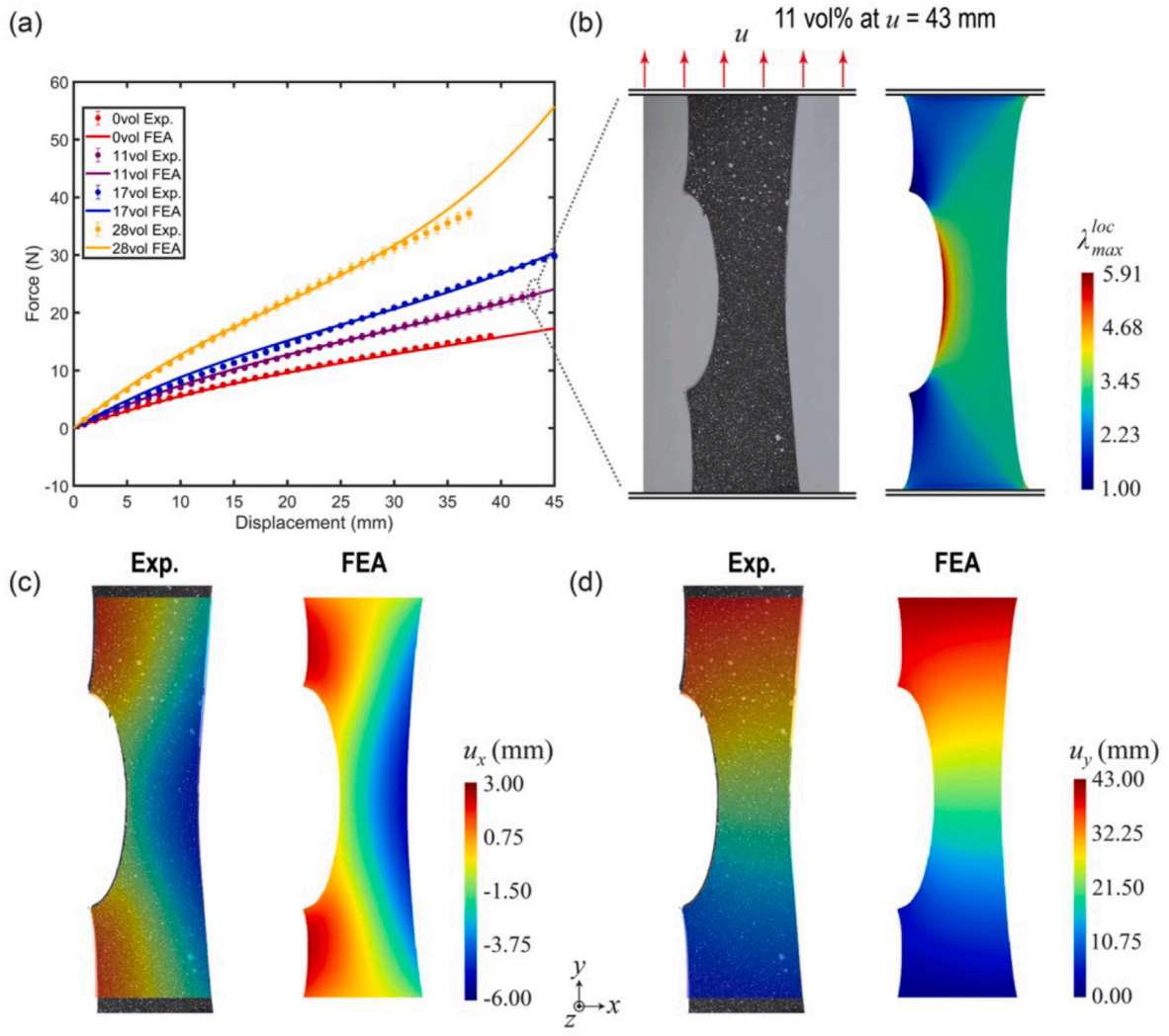

Fig. 4. Comparison of numerical and experimental results for the round-notched MRE specimen under tension. (a) Force–displacement (F–u) curves from experiments (markers with error bars) and FEA (solid lines) for MREs composed of 20:1 PDMS with 0, 11, 17, and 28 vol% NdFeB particles. Each experimental marker represents the average of at least three replicates. (b) Fabricated specimen with 11 vol% particles (left) and its corresponding simulated maximum stretch field (right) at $u = 43$ mm. (c)–(d) Comparisons of the horizontal (u_x) and vertical (u_y) displacement fields between DIC measurements and FEA predictions for the deformed configuration shown in (b).

key derivations from [33]. The perfectly incompressible formulation in (8) can be viewed as the limiting case of the nearly incompressible formulation by setting $\partial\phi_p/\partial\hat{p} = 0$ in $(B.5)_2$, which eliminates the dependency of r_p on $\hat{p}$.

To solve for the displacement $\mathbf{u}$ and the Lagrange multiplier $\hat{p}$, we convert the weak form in (8) into its matrix form. Applying the Newton–Raphson scheme yields the incremental equilibrium equation

$$\begin{bmatrix} \frac{\partial \mathbf{R}_u}{\partial \mathbf{U}} & \frac{\partial \mathbf{R}_u}{\partial \hat{\mathbf{P}}} \\ \frac{\partial \mathbf{R}_p}{\partial \mathbf{U}} & \frac{\partial \mathbf{R}_p}{\partial \hat{\mathbf{P}}} \end{bmatrix} \begin{bmatrix} \delta\mathbf{U} \\ \delta\hat{\mathbf{P}} \end{bmatrix} = - \begin{bmatrix} \mathbf{R}_u \\ \mathbf{R}_p \end{bmatrix}. \tag{9}$$

Here, $\mathbf{R}_u$ and $\mathbf{R}_p$ are the global residual vectors corresponding to r_u and r_p, respectively. $\mathbf{U}$ and $\hat{\mathbf{P}}$ are the global vectors of $\mathbf{u}$ and $\hat{p}$, respectively, while $\delta\mathbf{U}$ and $\delta\hat{\mathbf{P}}$ denote their corresponding updates. At each Newton iteration, we solve (9) for the increments $\delta\mathbf{U}$ and $\delta\hat{\mathbf{P}}$, and update the state variables via $\mathbf{U} \leftarrow \mathbf{U} + \delta\mathbf{U}$ and $\hat{\mathbf{P}} \leftarrow \hat{\mathbf{P}} + \delta\hat{\mathbf{P}}$ until convergence.

To numerically compute $\mathbf{U}$ and $\hat{\mathbf{P}}$, we employ the open-source finite element analysis (FEA) framework FEniCSx [28,34], which allows us to directly implement (8) while the matrix form in (9) is handled automatically in the backend. Subsequently, the computational domain is discretized with an unstructured mesh composed of hexahedral elements, each integrating over 8 Gauss points. The displacement field ($\mathbf{u}$) is approximated using continuous, element-wise trilinear basis functions (CG-1 elements), with degrees of freedom located at cell vertices. The Lagrange multiplier ($\hat{p}$) is discretized using discontinuous, element-wise constant functions (DG-0 elements), where degrees of freedom are located at cell centroids. This mixed-element formulation balances computational efficiency and accuracy, offering stable and convergent solutions at moderate cost compared to higher-order discretizations. The numerical results are presented in Section 3 alongside corresponding experimental data for validation.

3. Experimental validation of the computational framework

3.1. Fabrication of MREs

As introduced earlier, MREs are composed of a soft base matrix and rigid filler particles. In this study, the base material is PDMS (Dow Sylgard 184 Kit) from Thermo Fisher Scientific Inc. (Waltham, MA, USA). The rigid fillers are NdFeB particles from Magnequench (Indianapolis, IN, USA), with an average particle diameter of approximately 25 μm.

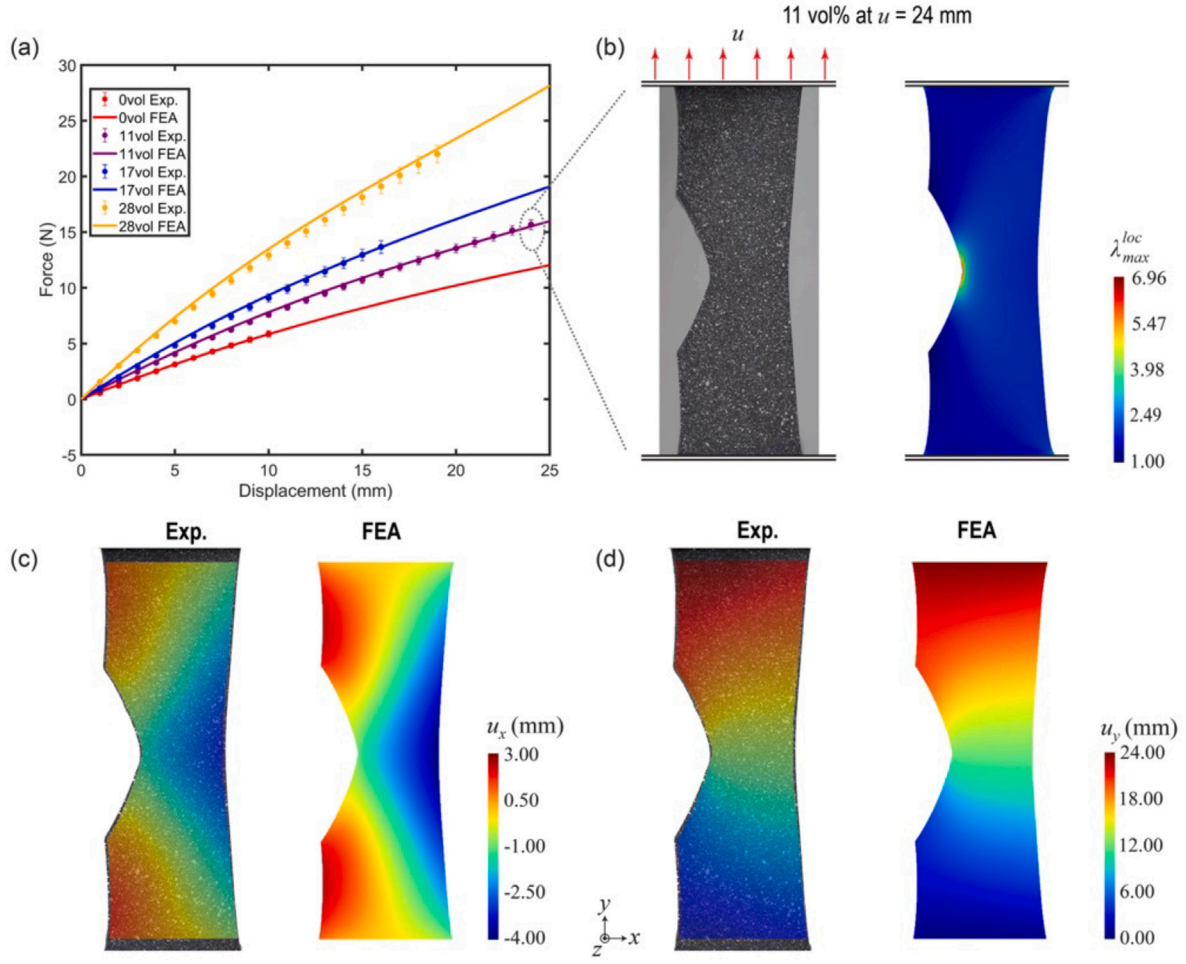

Fig. 5. Comparison of numerical and experimental results for the V-shaped-notched MRE specimen under tension. (a) Force–displacement (F–u) curves from experiments (markers with error bars) and FEA (solid lines) for MREs composed of 20:1 PDMS with 0, 11, 17, and 28 vol% NdFeB particles. Each experimental marker represents the average of at least three replicates. (b) Fabricated specimen with 11 vol% particles (left) and its corresponding simulated maximum stretch field (right) at u = 24 mm. (c)–(d) Comparisons of the horizontal (u_x) and vertical (u_y) displacement fields between DIC measurements and FEA predictions for the deformed configuration shown in (b).

The material synthesis procedure proceeds as follows. First, PDMS and NdFeB particles are thoroughly mixed for 15 min to ensure a homogeneous dispersion. The resulting mixture is then cast into 3D-printed polyethylene terephthalate glycol (PETG) molds, followed by a 1-hour degassing step to remove trapped air bubbles. The mixture is subsequently cured at 80 °C for 2 h. For tension samples, the cured material sheet is cut into dog-bone-shaped specimens according to the testing standards specified in [35]. For compression samples, the material is demolded in the shape defined by [36]. To ensure complete cross-linking and uniform post-curing effects across all samples, the specimens are stored at room temperature for 10 days prior to testing. Photographs of the fabricated specimens are shown in Fig. 1(a), where we observe that the PDMS sample appears nearly transparent, whereas the MRE sample is opaque black due to the embedded NdFeB particles.

To investigate the microstructure of the fabricated MREs, we present optical microscopy images in Fig. 1(b). These images correspond to a MRE sample containing 28 vol% NdFeB particles and are captured at two magnifications using a 3D laser scanning confocal microscope (VK-X1000, Keyence Corporation of America). The visualizations represent depth-integrated views of the particles, with different depths encoded by color. From these images, we observe that the NdFeB particles exhibit irregular morphologies and form a random yet relatively uniform spatial distribution within the PDMS matrix.

3.2. Uniaxial tension and compression tests with uniform strain states

We begin by introducing the uniaxial tension and compression tests. For these experiments, we prepare three groups of specimens with different base-to-agent ratios of PDMS, as summarized in Table 1. Within each group, we include four volume fractions (0%, 11%, 17%, and 28%) of NdFeB particles to assess the effect of particle reinforcement across compositions.

The uniaxial tension and compression tests are performed using a universal testing machine (Instron 68TM-30), equipped with 500 N and 30 kN load cells, respectively. All tests are conducted under a constant loading rate of 5 mm/min. For tension experiments, an extensometer is used to measure strain, and the samples are stretched until failure. In the compression tests, silicone oil is applied between the sample and fixture surfaces to minimize friction, and the samples are compressed to a maximum engineering strain of 25% to ensure uniform deformation. Compressive stress–strain data are directly obtained from the machine output.

To validate the predictive capability of our computational model, we compare the experimentally measured (first Piola–Kirchhoff) stress–stretch (S_1–$\bar{\lambda}$) responses with the theoretical predictions derived from (6). To enable this comparison, we first fit the model parameters (α_1,

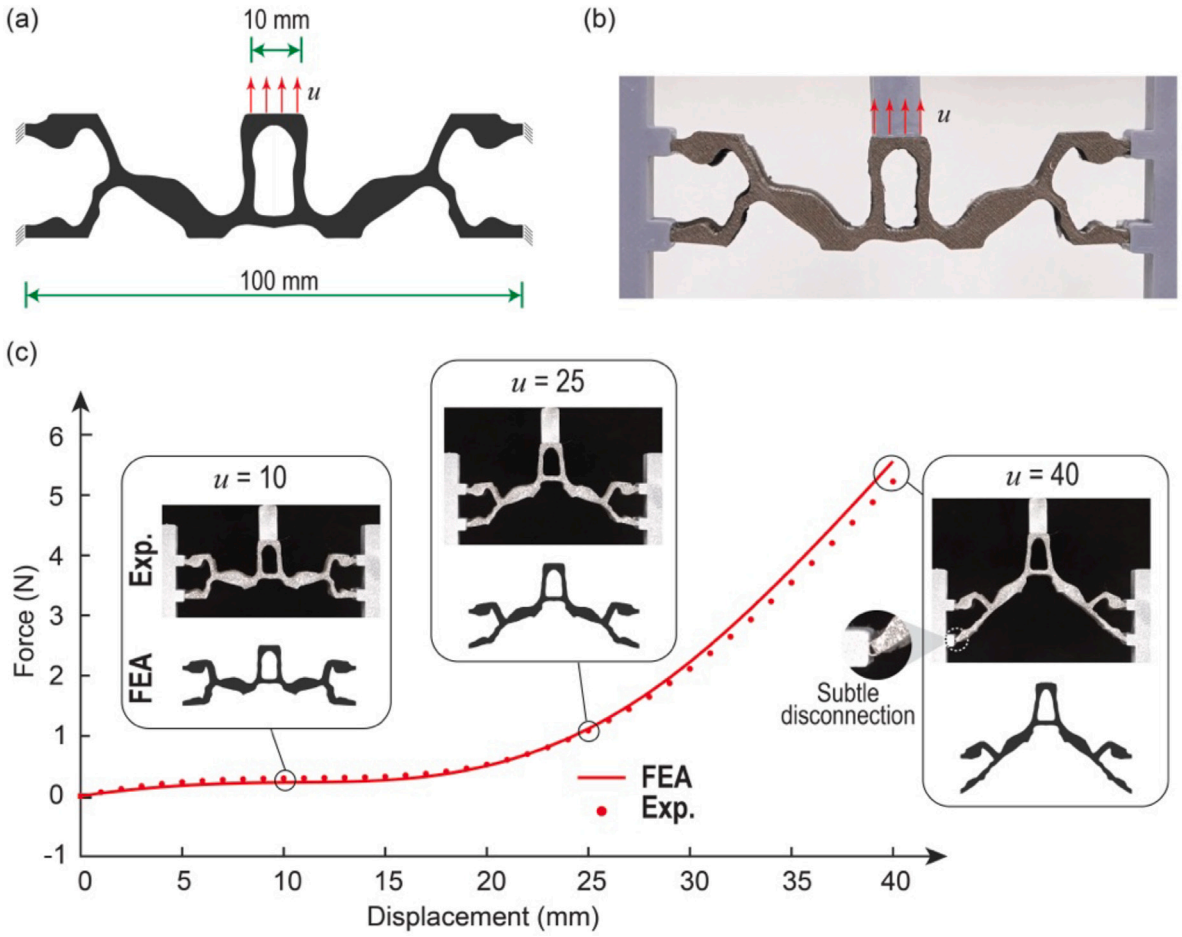

Fig. 6. Testing of the topologically optimized structure composed of 20:1 PDMS and 11 vol% NdFeB particles. (a) Rendering of the optimized design obtained via topology optimization. (b) Fabricated specimen mounted in a PLA frame for testing. (c) Comparison of numerical and experimental force–displacement (F–u) curves, with snapshots illustrating deformed configurations at key loading stages.

Table 1
Specifications of the specimens used in uniaxial tension and compression tests.

Group numbers	Base-to-agent ratios of PDMS	Particle fractions (vol%)
1	10:1	0, 11, 17, 28
2	20:1	0, 11, 17, 28
3	25:1	0, 11, 17, 28

Table 2
Fitted material constants for unfilled PDMS elastomers.

	α_1	α_2	μ_1 (MPa)	μ_2 (MPa)
Group 1 (10:1)	4.2996	−5.0028	0.4063	0.2107
Group 2 (20:1)	2.9798	−0.0783	0.0276	0.1478
Group 3 (25:1)	2.9440	−0.0698	0.0189	0.0682

α_2, μ_1, and μ_2) using the experimental S_1–$\bar{\lambda}$ curves of the unfilled PDMS samples (0 vol% NdFeB) in each group. For these fits, we set the particle concentration to $c = 0$ in (6). The calibrated material constants are listed in Table 2. Using these constants and the known particle fractions (c) in Table 1, we then compute the theoretical S_1–$\bar{\lambda}$ relations for each reinforced elastomer with (6).

The comparisons between the theoretical and experimental S_1–$\bar{\lambda}$ relations are shown in Fig. 2, and the key observations are as follows. First, the addition of NdFeB particles noticeably stiffens the PDMS elastomers, supported by the increasing magnitude of the first Piola–Kirchhoff stress (S_1) with higher particle fractions. Second, the theoretical and experimental S_1–$\bar{\lambda}$ relations generally exhibit good agreement, demonstrating the predictive accuracy of the material model described in (5)–(6).

Nonetheless, there are two exceptions. The first is the sample composed of 10:1 PDMS with 28 vol% NdFeB particles, the stiffest specimen in Group 1, which fractures prematurely due to limited material strength [37,38]. The second is the 10:1 PDMS specimen with 17 vol% particles, where the experimental stress response under large deformations falls below the theoretical prediction. This deviation is likely due to interfacial debonding between the matrix and particles, caused by insufficient adhesion at high strains.

3.3. Tension tests of notched specimens with localized strains

In this section, we focus on the mechanical responses of notched MRE specimens, where strain localizes around the notch front. The digital renderings and fabricated specimens are shown in Fig. 3. We test two types of notched specimens: one with a rounded notch (Fig. 3(a)) and the other with a V-shaped notch. Both types are fabricated using materials from Group 2 in Table 1, i.e., PDMS with a 20:1 base-to-agent ratio and particle volume fractions of 0, 11, 17, and 28 vol%.

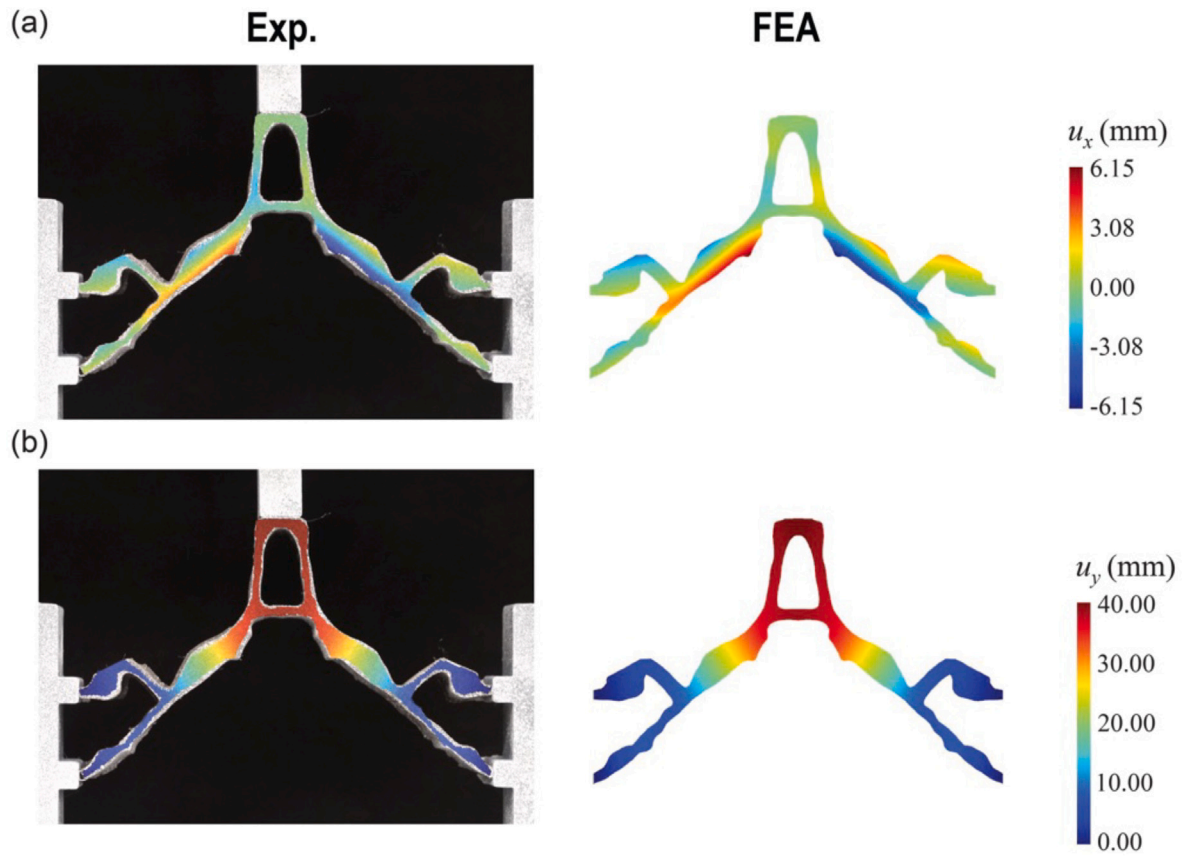

Fig. 7. Comparison of the (a) horizontal and (b) vertical displacement fields obtained from experiments (DIC) and simulations (FEA) for the topologically optimized specimen at an applied displacement of $u = 40$ mm.

The mechanical tests are performed by clamping the top and bottom of each specimen into the grips of a universal testing machine (Instron 68TM-30). The loading is conducted under displacement control (loading rate: 5 mm/min) through a 500 N load cell. Each test continues until fracture initiates at the notch front, at which point the force–displacement (F–u) data are recorded from the testing machine.

To capture the full-field displacement response, we apply digital image correlation (DIC). Prior to testing, speckle patterns are created on the specimen surfaces by spray painting. During loading, videos of the deformation process are recorded using a digital camera (Sony Alpha 7R III, Sony Corporation). Selected frames are extracted using MATLAB, and the displacement fields are computed using the open-source DIC software Ncorr [39].

The comparison between experimental and numerical results for the round-notched specimen is presented in Fig. 4. As shown in the force–displacement (F–u) curves in Fig. 4(a), the computational predictions align well with experimental data, except for the specimen containing 28 vol% particles, which fractures prematurely due to its high stiffness. This agreement again confirms the predictive accuracy of the proposed material model in (5) and the numerical implementation in Section 2.2, even under strain localization conditions (Fig. 4(b)). In addition to the global F–u response, we compare the local displacement fields in Fig. 4(c)–(d). The observed consistency between the experimental data and FEA-predicted displacements (u_x and u_y) demonstrates the model's ability to capture local deformation features.

A similar comparison for the V-shaped-notched specimen is shown in Fig. 5. Again, both the global force–displacement curves (Fig. 5(a)) and the local displacement fields (Fig. 5(c)–(d)) show good agreement. Notably, these results remain accurate even at large local stretches (with $\lambda_{\max}^{\text{loc}} = 6.96$ in Fig. 5(b)), highlighting the general applicability of the constitutive model.

3.4. Testing of a topologically optimized design

In this final test, we evaluate the performance of the proposed material model and its numerical implementation in capturing the behavior of a complex-shaped structure designed via topology optimization [40–42]. The digital rendering of the optimized design is shown in Fig. 6(a), and the fabricated specimen along with the experimental setup is presented in Fig. 6(b). The specimen is fabricated using 20:1 PDMS with 11 vol% NdFeB particles (Group 2 in Table 1), and has a thickness of 15 mm to limit out-of-plane deformation.

The specimen is clamped at both ends by a custom 3D-printed polylactic acid (PLA) loading frame. A vertical displacement (u) is applied to the top surface of the specimen at a constant rate of 5 mm/min. The corresponding force–displacement (F–u) relations are recorded, and snapshots of the deformed configurations are shown in Fig. 6(c) alongside the numerical predictions.

The experimental force–displacement curve exhibits a distinct two-stage behavior. During the initial loading phase ($u = 10$ to $u = 25$ mm), the overall stiffness remains low and forms a plateau region. This behavior results from the rotation-dominated deformation of structural members. As the displacement increases ($u = 25$ to $u = 40$ mm), the stiffness rises rapidly due to the onset of axial stretching in the members.

Additionally, the comparison between the experimental and numerical F–u responses reveals a good overall agreement, demonstrating the capability of the proposed material model to handle complex geometries. A minor deviation appears after $u = 30$ mm, due to slight disconnection between the specimen and the PLA loading frame.

To further validate the model, we compare the full-field displacement data at $u = 40$ mm in Fig. 7. Both the experimental and numerical results exhibit consistent displacement fields, confirming the accuracy

and generality of the constitutive model and its numerical implementation in predicting both global and local responses of complex MRE structures.

4. Concluding remarks

This work integrates a computational framework for the rapid prediction of the nonlinear elastic response of MREs, supported by systematic experimental validation on representative samples. The computational framework builds on the analytical homogenization model of [27] for general filled elastomers, combined with the effective shear modulus ratio from [19]. By construction, it requires only the material constants of the unfilled elastomer (α_1, α_2, μ_1, and μ_2) and the particle volume fraction (c). Consequently, it enables direct prediction of the nonlinear elastic response of MREs from a single measurement of the unfilled elastomer.

On the experimental side, we validate the framework using a series of non-magnetized MRE (PDMS–NdFeB) samples. These samples cover a range of matrix cross-link densities, filler concentrations (0%–28%), and specimen geometries, subjected to both uniform and highly localized strains. The measured responses consistently agree with the analytical and numerical predictions, thereby confirming the validity of the integrated framework.

This study advances the field in four aspects:

(i) The integrated computational framework, grounded in [19,27], offers a simple yet rigorous tool for predicting the macroscopic response of MREs across any physically admissible particle volume fraction. It requires only a single characterization of the elastomeric matrix, thereby avoiding repeated computational or experimental homogenization.

(ii) We present systematic experimental validation of the framework for MREs. These results also reaffirm the analytical homogenization approach in [25,27] for *general* filled elastomers, complementing the experimental findings in [26].

(iii) We numerically and experimentally investigate particle volume fractions from 0% to 28%, which exceed the commonly studied ranges in the literature — e.g., 5%–25% for numerical verification in [25] and 10% for experimental validation in [26]. This extension broadens the *validated* applicability of the analytical homogenization approach in [25,27].

(iv) The framework establishes a foundation for integration into coupled formulations [4,29,30], enabling rapid prediction of magneto-mechanical responses in magnetized MREs and accelerating the design of MRE-based structures such as magnetically actuated soft robots for biomedical applications.

Given the preliminary success of this study, an important extension is to experimentally examine the influence of different particle materials and diameters. The present work primarily focuses on a representative particle material (NdFeB) employed in [5,8]. Nevertheless, we anticipate that the nonlinear elastic responses predicted by (5), as well as the main conclusions of this study, are applicable to other *rigid* particles such as iron oxide. This expectation holds provided that the particle size remains at the micrometer scale — where the hydrodynamic effect serves as the only reinforcement mechanism introduced by the particles [26] — and is sufficiently small relative to the composite dimensions to ensure the validity of homogenization. Extending the experimental validation to a broader range of particle materials and sizes is an important direction for future work.

CRediT authorship contribution statement

Chao Wang: Writing – review & editing, Writing – original draft, Visualization, Validation, Software, Methodology, Investigation, Formal analysis, Data curation. **Yingqi Jia:** Writing – review & editing, Writing – original draft, Methodology, Investigation. **Arvin Ardebili Sharma:** Writing – review & editing, Investigation, Data curation. **Zhi Zhao:** Writing – review & editing, Methodology, Investigation. **Xiaojia Shelly Zhang:** Writing – review & editing, Writing – original draft, Supervision, Resources, Project administration, Methodology, Investigation, Funding acquisition, Conceptualization.

Declaration of competing interest

The authors declare that they have no known competing financial interests or personal relationships that could have appeared to influence the work reported in this paper.

Acknowledgments

The authors acknowledge the financial support from the U.S. Defense Advanced Research Projects Agency (DARPA) Young Faculty Award (N660012314013) and the U.S. National Science Foundation (NSF) CAREER Award CMMI-2047692 and NSF Award CMMI-2245251. Optical microscopy imaging was carried out in part in the Materials Research Laboratory Central Research Facilities, University of Illinois. The information provided in this paper is the sole opinion of the authors and does not necessarily reflect the view of the sponsoring agency.

Appendix A. Key steps for deriving the constitutive model in (7)

This section summarizes the key steps in deriving the constitutive model in (7), an approximate stored-energy function proposed in [25] for *non-Gaussian* elastomers reinforced with an isotropic distribution of rigid particles at *finite* concentrations. This approximation is further based on the solution in [24] for *Gaussian* elastomers containing a *dilute*, isotropic distribution of rigid particles. The key derivation steps for the constitutive model are outlined below.

A.1. Gaussian elastomers with a dilute distribution of rigid particles

We first consider a composite consisting of an incompressible isotropic elastomer and an isotropic distribution of rigid particles. The elastomer is modeled by the Gaussian stored-energy function

$$W_{\mathrm{e}}(I_1) = \frac{\mu}{2}(I_1 - 3),$$

where μ denotes the initial shear modulus. The rigid particles are idealized with a stored-energy function given in (2). The effective response of the two-phase composite, up to first order in the particle volume fraction c, is described by the stored-energy function [24]

$$\overline{W}(\bar{\lambda}_1, \bar{\lambda}_2; c) = \frac{\mu}{2}\left[\bar{\lambda}_1^{-2} + \bar{\lambda}_2^{-2} + (\bar{\lambda}_1\bar{\lambda}_2)^{-2} - 3\right] + 2\mu c H(\bar{\lambda}_1, \bar{\lambda}_2) + \mathcal{O}(c^2). \quad \text{(A.1)}$$

The function $H(\bar{\lambda}_1, \bar{\lambda}_2)$ accounts for the contribution of the rigid inclusions and satisfies a nonlinear Eikonal partial differential equation (PDE) [24]

$$H + \alpha_1(\bar{\lambda}_1, \bar{\lambda}_2)\left(\frac{\partial H}{\partial \bar{\lambda}_1}\right)^2 + \alpha_2(\bar{\lambda}_1, \bar{\lambda}_2)\left(\frac{\partial H}{\partial \bar{\lambda}_2}\right)^2 + \alpha_3(\bar{\lambda}_1, \bar{\lambda}_2)\frac{\partial H}{\partial \bar{\lambda}_1}\frac{\partial H}{\partial \bar{\lambda}_2} = 0$$

subject to

$$H(\bar{\lambda}, \bar{\lambda}) = 3\left\{\int_1^{\bar{\lambda}} z^{-3}|z^6 - 1|\left[1 + 2z^6 - \frac{3z^6}{\sqrt{1 - z^6}}\ln\left(\frac{1 + \sqrt{1 - z^6}}{z^3}\right)\right]^{1/2} \mathrm{d}z\right\}^2.$$

The coefficients α_1, α_2, and α_3 are functions of $\bar{\lambda}_1$ and $\bar{\lambda}_2$ with expressions provided in Appendix A of [24]. Note that $H(\bar{\lambda}_1, \bar{\lambda}_2)$ and consequently $\overline{W}(\bar{\lambda}_1, \bar{\lambda}_2; c)$ need to be determined numerically. It is convenient to approximate $\overline{W}$ as [24]

$$\widetilde{W}(\bar{I}_1; c) = \frac{\mu}{2}(\bar{I}_1 - 3) + \frac{5\mu c}{4}(\bar{I}_1 - 3). \quad \text{(A.2)}$$

A.2. Non-Gaussian elastomers with a finite concentration of rigid particles

Building on the approximate stored-energy function $\widetilde{W}$ in (A.2), which characterizes Gaussian elastomers with dilute particle distributions, we extend the formulation to non-Gaussian rubbers reinforced with isotropically distributed rigid particles at finite concentrations. The generalization procedure from [25] proceeds as follows.

According to iterated dilute homogenization theory [43], a dilute suspension with stored-energy function

$$\widehat{W}(\overline{I}_1;c) = W_{\mathrm{e}}(\overline{I}_1) + c\ \mathcal{G}(W_{\mathrm{e}}(\overline{I}_1),\overline{I}_1) + \mathcal{O}(c^2) \quad \text{for} \quad c \searrow 0 \tag{A.3}$$

can be generalized to finite $c \in [0,1]$ through the PDE

$$(1-c)\frac{\partial \widehat{W}_c(\overline{I}_1;c)}{\partial c} - \mathcal{G}(\widehat{W}_c(\overline{I}_1;c),\overline{I}_1) = 0$$

with initial condition

$$\widehat{W}_c(\overline{I}_1;0) = W_{\mathrm{e}}(\overline{I}_1).$$

Here, we recall that W_{e} denotes the stored-energy function of the neo-Hookean solid, $\overline{I}_1$ the macroscopic invariant, and c the particle volume fraction. The variables $\widehat{W}$ (typically known) and $\widehat{W}_c$ (to be determined) represent the stored-energy functions of reinforced elastomers for dilute and finite particle fractions, respectively. $\mathcal{G}$ denotes a function of W_{e} and $\overline{I}_1$.

Comparing the dilute form in (A.2) with the general form in (A.3), we identify

$$\mathcal{G}(\widehat{W}_c(\overline{I}_1;c),\overline{I}_1) = \frac{5}{2}\widehat{W}_c(\overline{I}_1;c).$$

Solving the PDE for $\widehat{W}_c(\overline{I}_1;c)$ yields the closed-form expression for the effective stored-energy function of reinforced Gaussian elastomers at finite particle concentrations. This expression reads as [25]

$$\widehat{W}_c(\overline{I}_1;c) = \frac{\mu}{2(1-c)^{5/2}}(\overline{I}_1 - 3).$$

Finally, applying the nonlinear comparison medium approach to $\widehat{W}_c(\overline{I}_1;c)$ leads to (7), which governs non-Gaussian matrices reinforced with finite concentrations of rigid particles.

Appendix B. Equilibrium equations for modeling nearly incompressible MREs

In this section, we present the equilibrium equations for modeling nearly incompressible MREs based on [33]. We consider a nearly incompressible MRE governed by the stored-energy function

$$\phi(\overline{I}_1,\overline{J};c) = \widetilde{\psi}_c(\overline{I}_1;c) + \phi_J(\overline{J};c),$$

where $\widetilde{\psi}_c(\overline{I}_1;c)$ corresponds to the first branch of (5), and the volumetric strain energy density ϕ_J is assumed to be *convex* in $\overline{J}$. Following the Legendre transformation, we introduce an auxiliary scalar field $\hat{p}$ and define the transformed stored-energy function as

$$\hat{\phi}(\overline{I}_1,\hat{p};c) = \max_{\overline{J}}\left[\hat{p}\ (\overline{J}-1) - \phi(\overline{I}_1,\overline{J};c)\right] = -\widetilde{\psi}_c(\overline{I}_1;c) + \phi_p\ (\hat{p};c)$$

with

$$\phi_p(\hat{p};c) = \max_{\overline{J}}\left[\hat{p}\ (\overline{J}-1) - \phi_J(\overline{J};c)\right], \tag{B.1}$$

where the expression $\hat{p}\ (\overline{J}-1) - \phi_J(\overline{J};c)$ is concave in $\overline{J}$ by construction.

Proposition 1. *The original (ϕ) and transformed ($\hat{\phi}$) stored-energy functions admit the dual relation of*

$$\phi(\overline{I}_1,\overline{J};c) = \max_{\hat{p}}\left[\hat{p}\ (\overline{J}-1) - \hat{\phi}(\overline{I}_1,\hat{p};c)\right]. \tag{B.2}$$

Proof. Stationarity of the maximand in (B.1) with respect to $\overline{J}$ yields the optimality condition as

$$\frac{\partial \phi_J}{\partial \overline{J}}(\overline{J}^*(\hat{p});c) = \hat{p},$$

which defines the maximizer $\overline{J}^*(\hat{p})$. Substituting $\overline{J}^*(\hat{p})$ into the maximand in (B.2) derives

$$\hat{p}\ (\overline{J}-1) + \widetilde{\psi}_c(\overline{I}_1;c) + \phi_J(\overline{J}^*(\hat{p});c) - \hat{p}\ (\overline{J}^*(\hat{p})-1). \tag{B.3}$$

Vanishing the first derivative of (B.3) with respect to $\hat{p}$ yields the equation of the maximizer $\hat{p}^*$ as

$$\begin{aligned} g(\hat{p}^*) = \overline{J} - 1 + \frac{\partial \phi_J}{\partial \overline{J}}(\overline{J}^*(\hat{p}^*);c)\frac{\partial \overline{J}^*}{\partial \hat{p}} - (\overline{J}^*(\hat{p}^*)-1) \\ - \hat{p}^*\frac{\partial \overline{J}^*}{\partial \hat{p}} = 0 \quad \Rightarrow \quad \overline{J}^*(\hat{p}^*) = \overline{J}. \end{aligned} \tag{B.4}$$

Finally, substituting (B.4) into (B.3) renders

$$\begin{aligned} &\hat{p}^*\ (\overline{J}-1) + \widetilde{\psi}_c(\overline{I}_1;c) + \phi_J(\overline{J}^*(\hat{p}^*);c) - \hat{p}^*\ (\overline{J}^*(\hat{p}^*)-1) \\ &\quad = \widetilde{\psi}_c(\overline{I}_1;c) + \phi_J(\overline{J};c) = \phi(\overline{I}_1,\overline{J};c), \end{aligned}$$

which proves (B.2) because $\hat{p}\ (\overline{J}-1) - \hat{\phi}(\overline{I}_1,\hat{p};c)$ is *concave* due to

$$\frac{\partial^2 \phi_J}{\partial \overline{J}^2}(\overline{J}^*(\hat{p}))\frac{\partial \overline{J}^*}{\partial \hat{p}} = 1 \quad \Rightarrow \quad \frac{\partial g}{\partial \hat{p}} = -\frac{\partial \overline{J}^*}{\partial \hat{p}} = -\left[\frac{\partial^2 \phi_J}{\partial \overline{J}^2}(\overline{J}^*(\hat{p}))\right]^{-1} < 0. \quad \square$$

Based on (B.2), the total potential energy of the system is expressed as

$$\Pi(\mathbf{u},\hat{p}) = \max_{\hat{p}}\int_{\Omega^0}\left[\hat{p}\ (\overline{J}-1) - \hat{\phi}(\overline{I}_1,\hat{p};c)\right]\mathrm{d}\mathbf{X} - \int_{\Omega^0}\overline{\mathbf{b}}\cdot\mathbf{u}\ \mathrm{d}\mathbf{X} - \int_{\partial\Omega^0_{\mathcal{N}}}\overline{\mathbf{t}}\cdot\mathbf{u}\ \mathrm{d}\mathbf{X}$$

subject to $\mathbf{u} = \overline{\mathbf{u}}$ on $\partial\Omega^0_D$. Applying the principle of minimum potential energy yields the Euler–Lagrange equations for $\mathbf{u}$ and $\hat{p}$ as

$$\begin{cases} \mathrm{Div}\left(2\widetilde{\psi}_{c,\overline{I}_1}\overline{\mathbf{F}} + \hat{p}\ \overline{J}\ \overline{\mathbf{F}}^{-\mathsf{T}}\right) + \overline{\mathbf{b}} = \mathbf{0} & \text{for } \mathbf{X}\in\Omega^0 \\ \mathbf{u} = \overline{\mathbf{u}} & \text{for } \mathbf{X}\in\partial\Omega^0_D \\ \left(2\widetilde{\psi}_{c,\overline{I}_1}\overline{\mathbf{F}} + \hat{p}\ \overline{J}\ \overline{\mathbf{F}}^{-\mathsf{T}}\right)\mathbf{N} = \overline{\mathbf{t}} & \text{for } \mathbf{X}\in\partial\Omega^0_{\mathcal{N}} \end{cases}$$

and

$$\overline{J} - 1 - \frac{\partial \phi_p}{\partial \hat{p}} = 0 \quad \text{for } \mathbf{X}\in\Omega^0,$$

where $\mathbf{N}$ is the unit outward normal of $\partial\Omega^0_{\mathcal{N}}$. Following a standard procedure, we reformulate the above Euler–Lagrange equations into their weak form as

$$\begin{cases} r_u(\mathbf{u},\hat{p}) = \int_{\Omega^0}\left(2\widetilde{\psi}_{c,\overline{I}_1}\overline{\mathbf{F}} + \hat{p}\ \overline{J}\ \overline{\mathbf{F}}^{-\mathsf{T}}\right) : \nabla\mathbf{v}\ \mathrm{d}\mathbf{X} \\ \quad - \int_{\Omega^0}\overline{\mathbf{b}}\cdot\mathbf{v}\ \mathrm{d}\mathbf{X} - \int_{\partial\Omega^0_{\mathcal{N}}}\overline{\mathbf{t}}\cdot\mathbf{v}\ \mathrm{d}\mathbf{X} = 0 \quad \forall\mathbf{v}\in\mathcal{K} \\ r_p(\mathbf{u},\hat{p}) = \int_{\Omega^0}\left(J - 1 - \frac{\partial \phi_p}{\partial \hat{p}}\right)\hat{q}\ \mathrm{d}\mathbf{X} = 0 \quad \forall\hat{q}\in\mathcal{Q} \end{cases} \tag{B.5}$$

subject to $\mathbf{u} = \overline{\mathbf{u}}$ on $\partial\Omega^0_D$.

Data availability

Data will be made available on request.

References

[1] K. Danas, S. Kankanala, N. Triantafyllidis, Experiments and modeling of iron-particle-filled magnetorheological elastomers, J. Mech. Phys. Solids 60 (1) (2012) 120–138.

[2] L. Bodelot, J.-P. Voropaieff, T. Pössinger, Experimental investigation of the coupled magneto-mechanical response in magnetorheological elastomers, Exp. Mech. 58 (2018) 207–221.

[3] Y. Kim, G.A. Parada, S. Liu, X. Zhao, Ferromagnetic soft continuum robots, Sci. Robot. 4 (33) (2019).

[4] R. Zhao, Y. Kim, S.A. Chester, P. Sharma, X. Zhao, Mechanics of hard-magnetic soft materials, J. Mech. Phys. Solids 124 (2019) 244–263.
[5] C. Wang, Z. Zhao, J. Han, A.A. Sharma, H. Wang, X.S. Zhang, Wireless magnetic robot for precise hierarchical control of tissue deformation, Adv. Sci. 11 (35) (2024) 2308619, http://dx.doi.org/10.1002/advs.202308619.
[6] J. Li, H. Chen, L. Wang, Model-guided navigation of magnetic soft guidewire for safe endovascular surgery, J. Mech. Phys. Solids 190 (2024) 105731.
[7] A.K. Bastola, L. Li, A new type of vibration isolator based on magnetorheological elastomer, Mater. Des. 157 (2018) 431–436.
[8] C. Wang, Z. Zhao, X.S. Zhang, Inverse design of magneto-active metasurfaces and robots: Theory, computation, and experimental validation, Comput. Methods Appl. Mech. Engrg. 413 (2023) 116065.
[9] Z. Zhao, X.S. Zhang, Topology optimization of hard-magnetic soft materials, J. Mech. Phys. Solids 158 (2022) 104628.
[10] M.A. Moreno-Mateos, M. Hossain, P. Steinmann, D. Garcia-Gonzalez, Hybrid magnetorheological elastomers enable versatile soft actuators, Npj Comput. Mater. 8 (1) (2022) 162.
[11] L. Wang, Co-design of magnetic soft robots with large deformation and contacts via material point method and topology optimization, Comput. Methods Appl. Mech. Engrg. 445 (2025) 118205.
[12] C. Wang, Z. Zhao, Z. Li, Y. Jia, A.A. Sharma, X.S. Zhang, Direct ink writing of magnetic soft materials with optimized printing path, Addit. Manuf. 105 (2025) 104770.
[13] K.A. Kalina, J. Brummund, P. Metsch, M. Kästner, D.Y. Borin, J. Linke, S. Odenbach, Modeling of magnetic hystereses in soft MREs filled with NdFeB particles, Smart Mater. Struct. 26 (10) (2017) 105019.
[14] C. Dorn, L. Bodelot, K. Danas, Experiments and numerical implementation of a boundary value problem involving a magnetorheological elastomer layer subjected to a nonuniform magnetic field, J. Appl. Mech. 88 (7) (2021).
[15] M.A. Moreno-Mateos, K. Danas, D. Garcia-Gonzalez, Influence of magnetic boundary conditions on the quantitative modelling of magnetorheological elastomers, Mech. Mater. 184 (2023) 104742.
[16] A. Saber, R. Sedaghati, On the modeling of magnetorheological elastomers: A state-of-the-art review, Adv. Eng. Mater. (2023).
[17] D. Mukherjee, K. Danas, A unified dual modeling framework for soft and hard magnetorheological elastomers, Int. J. Solids Struct. 257 (2022) 111513.
[18] D. Mukherjee, M. Rambausek, K. Danas, An explicit dissipative model for isotropic hard magnetorheological elastomers, J. Mech. Phys. Solids 151 (2021) 104361.
[19] V. Lefèvre, O. Lopez-Pamies, The effective shear modulus of a random isotropic suspension of monodisperse rigid n-spheres: From the dilute limit to the percolation threshold, Extrem. Mech. Lett. 55 (2022) 101818.
[20] H.M. Smallwood, Limiting law of the reinforcement of rubber, J. Appl. Phys. 15 (11) (1944) 758–766.
[21] R. Hill, On constitutive macro-variables for heterogeneous solids at finite strain, Proc. R. Soc. A 326 (1565) (1972) 131–147.
[22] D. Talbot, J. Willis, Variational principles for inhomogeneous non-linear media, IMA J. Appl. Math. 35 (1) (1985) 39–54.
[23] S. Müller, Homogenization of nonconvex integral functionals and cellular elastic materials, Arch. Ration. Mech. Anal. 99 (3) (1987) 189–212.
[24] O. Lopez-Pamies, T. Goudarzi, T. Nakamura, The nonlinear elastic response of suspensions of rigid inclusions in rubber: I—An exact result for dilute suspensions, J. Mech. Phys. Solids 61 (1) (2013) 1–18.
[25] O. Lopez-Pamies, T. Goudarzi, K. Danas, The nonlinear elastic response of suspensions of rigid inclusions in rubber: II—a simple explicit approximation for finite-concentration suspensions, J. Mech. Phys. Solids 61 (1) (2013) 19–37.
[26] M. Leonard, N. Wang, O. Lopez-Pamies, T. Nakamura, The nonlinear elastic response of filled elastomers: Experiments vs. Theory for the basic case of particulate fillers of micrometer size, J. Mech. Phys. Solids 135 (2020) 103781, http://dx.doi.org/10.1016/j.jmps.2019.103781.
[27] V. Lefèvre, O. Lopez-Pamies, Nonlinear electroelastic deformations of dielectric elastomer composites: II — non-Gaussian elastic dielectrics, J. Mech. Phys. Solids 99 (2017) 438–470, http://dx.doi.org/10.1016/j.jmps.2016.07.005.
[28] I.A. Baratta, J.P. Dean, J.S. Dokken, M. Habera, J.S. Hale, C.N. Richardson, M.E. Rognes, M.W. Scroggs, N. Sime, G.N. Wells, DOLFINx: The next generation FEniCS problem solving environment, 2023, http://dx.doi.org/10.5281/zenodo.10447666.
[29] M. Rambausek, D. Mukherjee, K. Danas, A computational framework for magnetically hard and soft viscoelastic magnetorheological elastomers, Comput. Methods Appl. Mech. Engrg. 391 (2022) 114500.
[30] K. Danas, A unified theoretical modeling framework for soft and hard magnetorheological elastomers, in: Electro-and Magneto-Mechanics of Soft Solids: Constitutive Modelling, Numerical Implementations, and Instabilities, Springer, 2024, pp. 59–139.
[31] O. Lopez-Pamies, A new I1-based hyperelastic model for rubber elastic materials, C. R. Mec. 338 (1) (2010) 3–11.
[32] H. Brinkman, The viscosity of concentrated suspensions and solutions, J. Chem. Phys. 20 (4) (1952) 571, http://dx.doi.org/10.1063/1.1700493.
[33] H. Chi, C. Talischi, O. Lopez-Pamies, G. H. Paulino, Polygonal finite elements for finite elasticity, Internat. J. Numer. Methods Engrg. 101 (4) (2015) 305–328.
[34] Y. Jia, C. Wang, X.S. Zhang, FEniTop: A simple fenicsx implementation for 2D and 3D topology optimization supporting parallel computing, Struct. Multidiscip. Optim. 67 (2024) 140, http://dx.doi.org/10.1007/s00158-024-03818-7.
[35] ASTM-D412, Standard test methods for vulcanized rubber and thermoplastic elastomers-tension, ASTM Int. (2016).
[36] ASTM-D575, Standard test methods for rubber properties in compression, ASTM Int. (2018).
[37] Y. Jia, O. Lopez-Pamies, X.S. Zhang, Controlling the fracture response of structures via topology optimization: From delaying fracture nucleation to maximizing toughness, J. Mech. Phys. Solids 173 (2023) 105227, http://dx.doi.org/10.1016/j.jmps.2023.105227.
[38] Y. Jia, R.D. Kundu, X.S. Zhang, Stress-constrained versus fracture-based topology optimization: A comparative study, Comput. Methods Appl. Mech. Engrg. 441 (2025) 117949, http://dx.doi.org/10.1016/j.cma.2025.117949.
[39] J. Blaber, B. Adair, A. Antoniou, Ncorr: open-source 2D digital image correlation matlab software, Exp. Mech. 55 (6) (2015) 1105–1122, http://dx.doi.org/10.1007/s11340-015-0009-1.
[40] M.P. Bendsøe, N. Kikuchi, Generating optimal topologies in structural design using a homogenization method, Comput. Methods Appl. Mech. Engrg. 71 (2) (1988) 197–224, http://dx.doi.org/10.1016/0045-7825(88)90086-2.
[41] M.P. Bendsoe, O. Sigmund, Topology Optimization: Theory, Methods, and Applications, Springer Science & Business Media, 2003.
[42] Z. Zhao, X.S. Zhang, Encoding reprogrammable properties into magneto-mechanical materials via topology optimization, Npj Comput. Mater. 9 (1) (2023) 57.
[43] O. Lopez-Pamies, An exact result for the macroscopic response of particle-reinforced neo-Hookean solids, J. Appl. Mech. 77 (021016) (2009) http://dx.doi.org/10.1115/1.3197444.